1 **Technical Note: Monitoring discharge of mountain streams by**

2 **retrieving image features with deep learning**

3 Chenqi Fang[1], Genyu Yuan[1], Ziying Zheng[1], Qirui Zhong[1], Kai Duan[1*]

4 *[1] School of Civil Engineering, Sun Yat-Sen University, Guangzhou, China*

5 *Corresponding author, E-mail: duank6@mail.sysu.edu.cn

Abstract

Traditional discharge monitoring usually relies on measuring flow velocity and cross-section area with various velocimeters or remote-sensing approaches. However, the topography of mountain streams in remote sites largely hinders the applicability of velocity-area methods. We here present a method to continuously monitor mountain stream discharge using a low-cost commercial camera and deep learning algorithm. A procedure of automated image categorization and discharge classification was developed to extract information on flow patterns and volumes from high-frequency red–green–blue (RGB) images with deep convolutional neural networks (CNNs). The method was tested at a small, steep, natural stream reach in southern China. Reference discharge data was acquired from a V-shaped weir and ultrasonic flowmeter installed a few meters downstream of the camera system. Results show that the discharge-relevant stream features implicitly embedded in RGB information can be effectively recognized and retrieved by CNN to achieve satisfactory performance in discharge measurement. Coupling CNN and traditional machine learning models (e.g., support vector machine and random forest) can potentially synthesize individual models' diverse merits and improve generalization performance. Besides, proper image pre-processing and categorization are critical for enhancing the robustness and applicability of the method under environmental disturbances (e.g., weather and vegetation on river banks). Our study highlights the usefulness of deep learning in analyzing complex flow images and tracking flow changes over time, which provides a reliable and flexible alternative

27   apparatus for continuous discharge monitoring of rocky mountain streams.

28   **Keywords**:

29   Discharge monitoring; Mountain streams; Deep learning; Machine learning; Image

30   categorization

31   1 Introduction

32   Continuous discharge data is critical for hydrological model development and flood

33   forecast (Clarke, 1999; Mcmillan et al., 2010), water resources management (Council,

34   2004), and aquatic ecosystem health assessment (Carlisle et al., 2017). Traditional

35   discharge monitoring relies on stream gauges that convert water level to discharge with

36   an established stage-discharge curve, or information on stable cross-sections and flow

37   velocity obtained from flow velocimeters such as acoustic doppler current profiler

38   (ADCP) and ultrasonic defectoscope (Kasuga et al., 2003). However, these approaches

39   require significant investment on the implementation of equipments, training of

40   personnel with expertise, and constant maintenance (Fujita et al., 2007; Czuba et al.,

41   2017; Yorke and Oberg, 2002). Besides, the performance of transducers and

42   velocimeters is usually susceptible to sediments and floating debris, particularly in

43   flooding seasons (Hannah et al., 2011). Consequently, large temporal gaps remain in

44   many discharge records across the world despite of the growing demand on data

45   (Davids et al., 2019; Royem et al., 2012). Spatially, flow monitoring of downstream

46   river sections has been assigned to a higher priority due to the concerns on water supply

47   and flood control, leading to an acute shortage of discharge data in mountain streams

48 and headwater catchments (Deweber et al., 2014).

49   To overcome the limitations of traditional methods, a few image-based approaches

50 have been introduced into water stage, flow velocity, and discharge measurement in

51 rivers (Noto et al., 2022; Leduc et al., 2018). Image-based (Leduc et al., 2018; Noto et

52 al., 2022) approaches rely only on the acquisition of digital images of streams from

53 inexpensive commercial cameras and thus have been a promising alternative for

54 continuous, noninvasive, and low-cost streamflow monitoring. The two most

55 commonly used approaches include large-scale particle image velocimetry (LSPIV)

56 and particle tracking velocimetry (PTV). LSPIV (Fujita et al., 2010) is based on a high-

57 speed cross-correlation scheme between an interrogation area (IA) in a first image and

58 IAs within a search region (SR) in a second image. The technique has been proved

59 effective in monitoring low-velocity and shallow-depth flow fields (Tauro et al., 2018).

60 However, it performs poorly in mapping velocity fields in high resolution when there

61 is a lacking of seeds on the water surface because the algorithm obtains the average

62 speed of each SR (Tauro et al., 2017). Compared to LSPIV, PTV was designed for low

63 seeding density flows, focusing on particle tracking instead of recognition. The PTV

64 approach does not require assumptions on flow steadiness nor the relative position of

65 neighbor particles (Tauro et al., 2018). Several algorithms have been developed for PTV

66 analysis, such as space-time image velocimetry (STIV) and optical tracking

67 velocimetry (OTV), overcoming the over-dependence on natural particles' shape and

68 size (Tauro et al., 2018; Tsubaki, 2017). STIV evaluates surface flow velocity by

69   analyzing a texture angle within a variation of brightness or color on the water surface,

70   while OTV combines automatic feature detection, Lucas-Kanade tracking algorithm

71   and track-based filtering methods to estimate subpixel displacements (Fujita et al., 2007;

72   Karvonen, 2016). Existing image-based discharge measurement methods all use the

73   velocity-area method to indirectly deduce discharge after identifying stage and average

74   (Davids et al., 2019; Leduc et al., 2018; Tsubaki, 2017; Herzog et al., 2022) velocity.

75   The average velocity in a cross-section is estimated with surface velocity derived from

76   natural or artificial seeds on water surface and pre-defined empirical relationships

77   between the surface velocity and average velocity. The velocity-area method relies on

78   a stable relationship between stage and cross-sectional area, and needs to take velocity

79   extrapolations to the edges and vertical distributions throughout the cross-section into

80   account (Le Coz et al., 2012). However, it is difficult to identify the water stage and

81   vertical characteristics of mountain streams due to the steep, narrow, and highly

82   heterogeneous cross-sections. The applicability of PIV and PTV approaches is largely

83   hindered by such topography.

84   Unlike PIV and PTV, deep learning models possess the capability to extract

85   discharge-related features from images of rivers or streams automatically. These models

86   are able to adjust the weights assigned to each feature, eliminating the need for manual

87   attention and reducing the risk of overemphasizing or misinterpreting features that are

88   unresponsive to flow discharge (Canziani et al., 2016). Besides, deep learning models

89   can extract low-level image features, such as edges, textures, and colors (Jiang et al.,

90 2021). These merits could be essential in retrieving information from images of

91 mountain streams, particularly in regions with intricate cross-sectional profiles.

92 In this study, we propose a novel mountain stream discharge monitoring method

93 using a low-cost commercial camera and deep learning models. Automated image

94 categorization and pre-processing procedures were developed for processing high-

95 frequency red–green–blue (RGB) images, and then the convolutional neural network

96 (CNN) was used to extract information on flow patterns from RGB matrixes and

97 establish empirical relationships with the classification probabilities of discharge

98 volumes. We hypothesize that (1) the features of mountain streams (e.g., coverage of

99 water surface, flow direction, flow velocity) embedded in RGB images can be

100 recognized by suitable deep learning approaches to achieve effective discharge

101 monitoring, and (2) proper image pre-processing and categorization can improve

102 accuracy of image-based discharge monitoring of mountain streams. A rocky mountain

103 stream of a headwater catchment in tropical southern China was used as a study site to

104 test our hypotheses.

105

106 **2 Methods**

107 **2.1 Site and field setting**

108 The study site is located on a small, steep, rocky reach of a stream in the Zhuhai Campus

109 of Sun Yat-sen University, China (22°20′58″ N, 113°34′29″ E). The site elevation is 13

110 m above sea level and about 2 km away from the Lingding Yang of South China Sea.

111 The stream flow is mainly controlled by rainfall in the upstream drainage area. Water

112 stage and flow velocity increase rapidly during East Asian summer monsoon rainfalls

113 and fluctuate with synoptic weather conditions on dry days.

114   The main objective of the study was to test the applicability of deep-learning based

115 image processing approaches in capturing the flow characteristics and discharge

116 volumes in the daily flow cycle in this mountain stream. We selected a straight, single-

117 thread reach for the gauging location, and set up a Hikvision camera on the left bank of

118 the stream to collect flow images (**Fig. 1**). Discharge data monitored by a weir about 8

119 m downstream of the camera was used for model training and validation. The camera

120 was installed 3 m above the ground, facing the surface of the stream almost vertically.

121 The entire stream width is visible in the images. The camera was equipped with a 150W

122 solar panel and 80AH lithium battery, enabling the camera to work continuously for 80

123 hours without external power on rainy days. The camera supports the wireless

124 transmission of video data to the server.

125

126

127 **Figure 1.** Camera setup. The camera is set on the left bank of the stream, about 3 m

128 above the water surface, and 8 m upstream of a gauging weir.

129

130 ## 2.2 Data

131 The flat V-shaped weir downstream of the camera monitors discharge with an open

132 channel flowmeter and an overflow flowmeter. The flowmeters measure water levels in

133 the channel and in front of the weir with ultrasonic sensors and calculate real-time

134 discharge at the time step of two minutes by a semi-empirical equation suggested by

135 the State Bureau of Technical Supervision of China (www.chinesestandard.net), as

136
$$Q = \frac{8}{15} C_e \tan\frac{\theta}{2} \sqrt{2g} h_e^{\frac{5}{2}} \tag{1}$$

137 where Q is the discharge of stream, θ is the angle of triangular weir, g is

138   acceleration of gravity, h_e is the height of the water surface from the bottom of triangle

139   barrier, C_e is an empirical coefficient.

140   We collected the discharge data of the weir and its corresponding stream videos

141   during daylight (07:00-19:00 UTC+8) from July 20th to September 27th, 2022. The raw

142   video resolution was 2560×1440 pixels with a refresh rate of 50 Hz. Images were

143   extracted from the videos at 5-minute intervals to avoid excessive similarity between

144   adjacent images. A total of 7,757 image samples labeled with 37 discharge values

145   between 0.014 and 0.050 m³/s at the interval of 0.001 m³/s were collected for model

146   testing.

147   **2.3 Image processing**

148   **2.3.1 Image categorization**

149   Environmental disturbances such as illumination and shadow can seriously interfere

150   with the extraction of effective image features of mountain streams, such as boundaries

151   of water surface and textures of flow lines (Herzog et al., 2022; Gershon et al., 1986).

152   Although researchers have proposed methods to eliminate shadows (Finlayson et al.,

153   2002), the treatment effect in some complex environments, such as plant shadows and

154   boulders distributed on mountain streams, is not always satisfactory.

155   Frequently observed disturbances on images include: (1) shadows in the target stream

156   region due to plants blocking direct sunlight; (2) image noise due to raindrops attached

157   to the camera lens on rainy days; (3) the lack of light leading to low brightness and

158   contrast of the image; (4) overexposure of image due to light reflection of the water

159 surface (around 16:00 UTC+8 in this case). Taking these factors into consideration, we

160 divided all image samples into six categories, including "Good quality", "Raindrops",

161 "Middle shadow", "Below shadow", "Water reflection", and "Dark" (**Fig. 2**). "Good

162 quality" contains image samples without obvious noise or shadow. All the other images

163 lose some feature information due to noise, shadows, reflections, or dim lighting. To

164 ensure the model performance under different environmental conditions, we designed

165 an automated categorization procedure (**Fig. 3**) to screen the raw images and exclude

166 the "Raindrops" and "Dark" samples from model training.

167

168
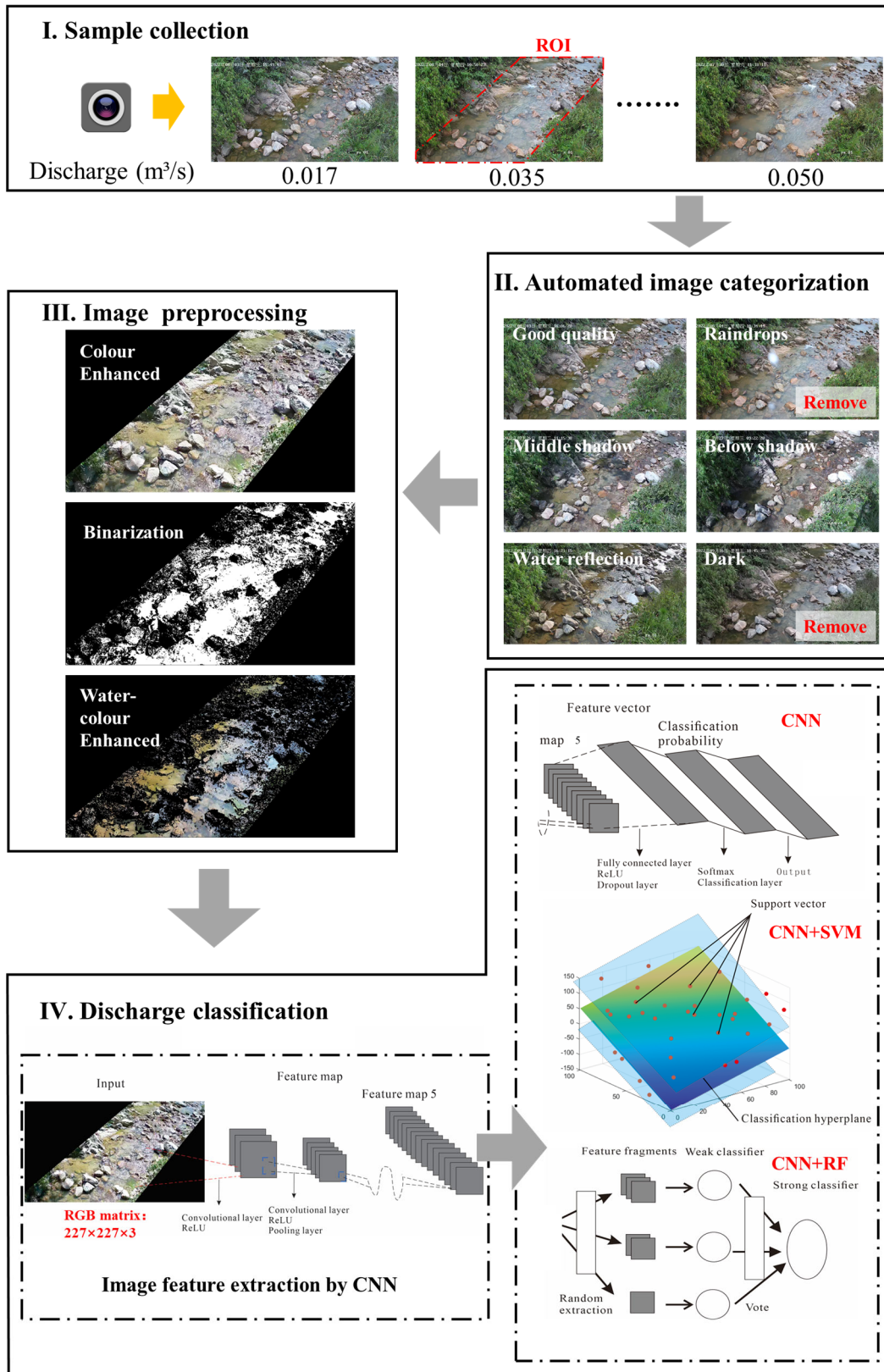
Figure 2. Flowchart of image processing and discharge monitoring.

170
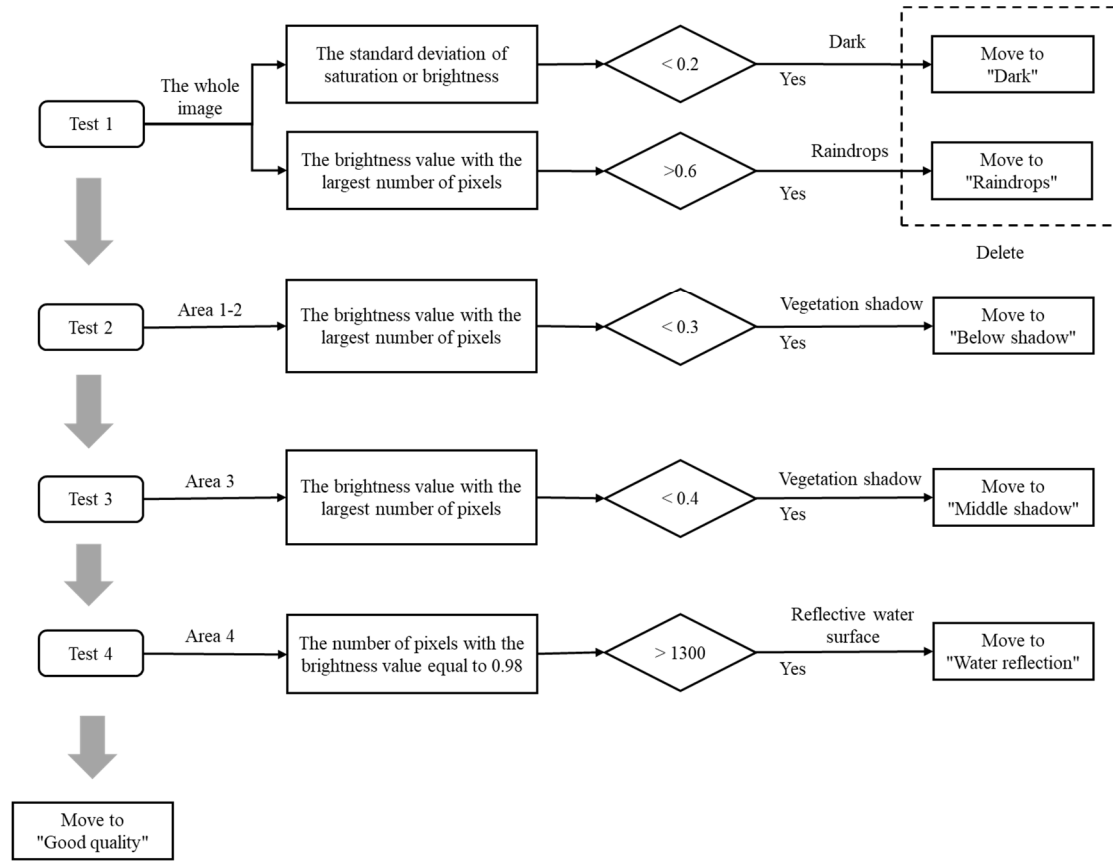
171

172   **Figure 3.** Procedure of automated image categorization.

173

174   Firstly, we selected four areas in the image as the detection areas (**Fig. 4a**) where the

175   special conditions mentioned above commonly occurred: the upper and lower shadows

176   in the target stream section mainly appeared in Area 3 and Area 1&2, respectively;

177   disturbance of water surface reflection was mostly found in Area 4. Then, the thresholds

178   of saturation or brightness in the four detection areas for image categorization were

179   determined manually by comparing image samples under different conditions. The

180   four-step procedure includes: (1) "Dark" images (**Fig. 4f-2**) were identified when the

181   standard deviation of the brightness or saturation of the full image was less than 0.2. (2)

182   "Raindrops" images (**Fig. 4f-3**) were identified when the brightness of the whole image

183   with the largest number of pixels was greater than 0.6. These two types of images were

184   excluded from the training samples. (3) "Below shadow" (**Fig. 4b-2**; **Fig. 4c-2)** and

185   "Middle shadow" images (**Fig. 4d-2**) were identified when the brightness value with

186   the largest number of pixels in Area 1&2 and Area 3 was less than 0.3 and 0.4,

187   respectively. (4) "Water reflection" images were identified when the number of pixels

188   with a brightness value of 0.98 in Area 4 exceeded 1300 (**Fig. 4e-2**). The images passing

189   all the tests in the procedure were considered "Good quality" samples. The other charts

190   in **Fig. 4** show the saturation and brightness distributions derived from a typical "Good

191   quality" image.
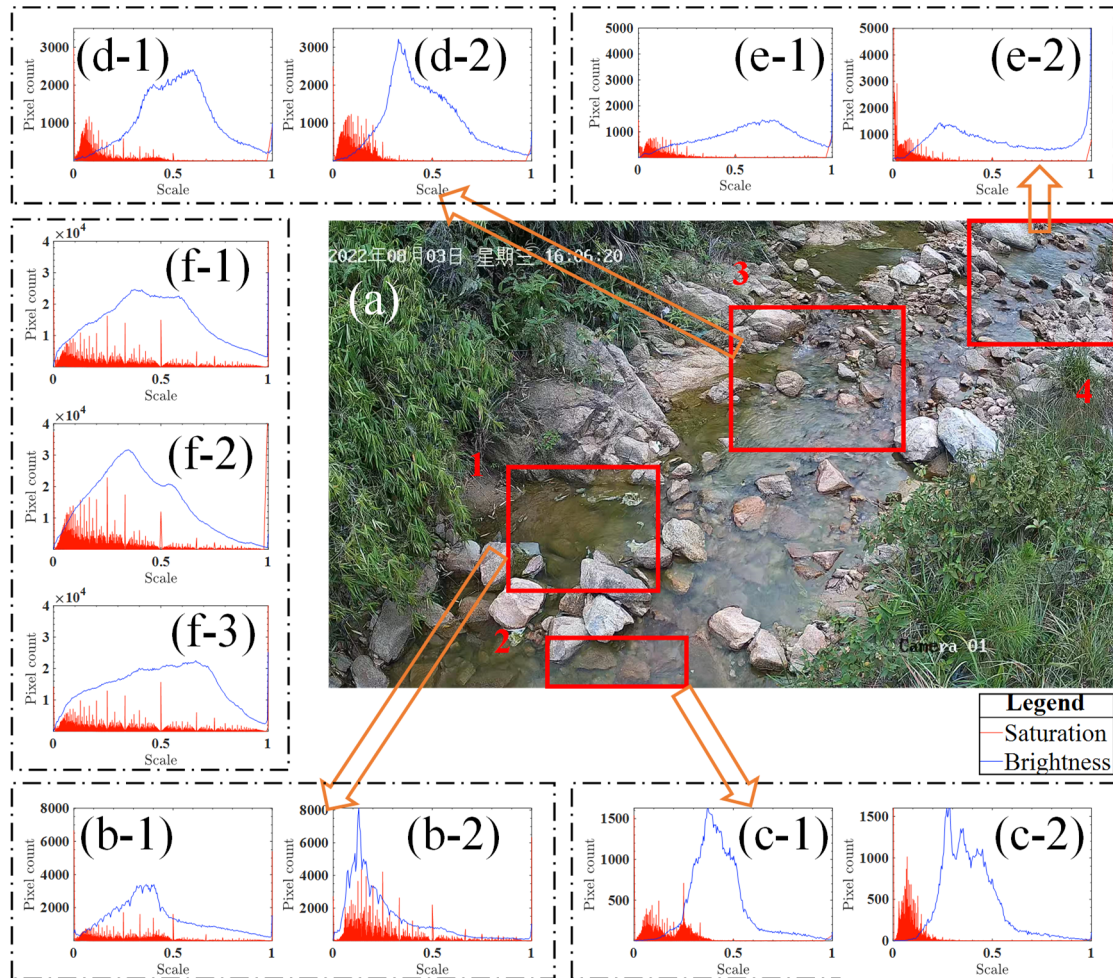
Figure 4. Comparison of saturation and brightness distributions in the four detection areas under different environmental conditions. The horizontal axis is the interval range (0-1) of saturation and brightness in HSB space. The vertical axis indicates the number of pixels under a certain saturation or brightness value. Figures b-1, c-1, d-1, and e-1 display the saturation and brightness distributions in Area 1-4 of a "Good quality" sample. Figures b-2, c-2, d-2, and e-2 display the results derived from samples of "Below shadow" (b-2; c-2), "Middle shadow" (d-2), and "Water reflection" (e-2), respectively. Figures f-1, f-2, and f-3 display the saturation and brightness distributions of an entire image, derived from "Good quality", "Dark", and "Raindrops" samples,

202 respectively.

203

204 **2.3.2 Color enhancement**

205 In order to highlight the stream features embedded in the images and avoid image

206 information redundancy, we compared three commonly used color enhancement

207 approaches to process the image samples.

208 **(1) Color Enhanced.** A dynamic histogram equalization technique (Abdullah-Al-

209 Wadud et al., 2007; Cheng and Shi, 2004) was used to enhance contrast and emphasize

210 stream features. First, vegetation areas on both sides of the stream were cropped and

211 filled with black. Then, histogram equalization was used to enhance the contrast

212 between light and dark, i.e., brighten the bubbles, swirls, ripples, splashes, water

213 coverage, etc., and darken the bottom stones and reflections in the water.

214 **(2) Binarization.** Binarization of image information can decrease the

215 computational load and enable the utilization of simplified methods compared to 256

216 levels of grey-scale or RGB color information (Finlayson et al., 2002; Sauvola and

217 Pietikäinen, 2000). In this case, the RGB and HSB (Hue, Saturation, Brightness)

218 information extracted from images suggests that the brightness of the stream water

219 under daylight ranges from 0.2 to 0.7, and the values of three color components follow:

220 $$R(x,y) + G(x,y) + B(x,y) > 350 \tag{2}$$

221 Where $R(x,y)$, $G(x,y)$ and $B(x,y)$ respectively represent the red, green, and blue

222 color values of the pixel (x, y). The original image was transformed into a binary image

223 by assigning the values of "1" and "0" to the pixels within and out of the water body,

224 respectively.

225 **(3) Water-color Enhanced.** Considering that water-color features may carry some

226 useful information on discharge (Kim et al., 2019), we tested a new pre-processing

227 method combining the two approaches above. The RGB information of the original

228 image within the water body areas was kept unchanged, while the non-water body areas

229 were filled with black color. Then, the water body areas were further enhanced with the

230 histogram equalization method to highlight the edge transition between the water body

231 and the background (Abdullah-Al-Wadud et al., 2007).

232 **2.3.3 Image denoising**

233 Images pre-processed by all of three approaches still contain large amounts of noise

234 due to environmental disturbances and edge oversharpening caused by image contrast

235 enhancement (Herzog et al., 2022). Therefore, the wavelet transform (Zhang, 2019)was

236 adopted to denoise the image samples. We chose a compromise threshold between hard

237 and soft thresholds as the threshold function (Chang et al., 2010). When the wavelet

238 coefficient is greater than or equal to the threshold, a compromise coefficient α ranging

239 from 0 to 1 is added before the threshold to achieve a smooth transition from hard to

240 soft thresholds, as

241 $$\lambda = \frac{median(d_j(k))}{0.6745} \times \sqrt{2\log(M \times N)} \tag{3}$$

242 $$\omega_\lambda = \begin{cases} [sign(\omega)](|\omega| - \alpha\lambda), |\omega| \geq \lambda \\ 0, |\omega| \geq \lambda \end{cases} \tag{4}$$

243 where j is the scale of wavelet decomposition, $d_j(k)$ is the coefficient of wavelet

244   decomposition, M and N are the length and width of images, ω is the wavelet

245   coefficient, λ is the set threshold, and $sign$ is the sign function. In this case, $M\times$

246   N=2560×1440, α=0.5.

2.4 Correlation between color information and discharge

248   The unstructured image data of mountain streams implicitly contains many stream

249   features relevant to discharge, such as the width and depth of streams, the coverage of

250   water surface, and spatial distributions of flow direction and flow velocity. CNN has

251   been widely used in various classification and regression problems for its capability in

252   recognizing the features of interest from images (Krizhevsky et al., 2017). In this study,

253   we attempted to achieve discharge monitoring by establishing empirical relationships

254   between the RGB color information of the water body and the discharge volumes. We

255   first explored the correlation between the combination of R/G/B values in the region of

256   interest (ROI, see **Fig. 2**) and the discharge conditions. Spearman's rank correlation

257   coefficient between RGB values and discharge is calculated as

$$r_s = 1 - \frac{6\sum_{i=1}^{n} d_i^2}{n(n^2-1)} \tag{5}$$

259   where n is the number of samples, d_i is the difference between the ranks of R/G/B values

260   and discharge of each image sample.

261

2.5 Algorithms of discharge estimation

263   We used three algorithms to establish discharge classification models (**Fig. 2**), including

264   convolutional neural network (CNN), support vector machine (SVM), and random

265   forest (RF). The data of the RGB color matrix derived from pre-processed images was

266   used as model inputs. SVM and RF were coupled with CNN to explore the potential

267   merits of traditional machine learning algorithms in improving the accuracy and

268   efficiency of CNN-based discharge classifiers. All the embedding image features are

269   normalized and regularized before passed to classifiers to avoid overfitting for CNN-

270   based models.

271   **2.5.1 Convolutional Neural Network (CNN)**

272   Deep convolutional neural network allows computational models composed of multiple

273   processing layers to learn representations of data with multiple levels of abstraction,

274   which have brought breakthroughs in processing images, video, speech, and audio

275   (Lecun et al., 2015). The AlexNet architecture (Krizhevsky et al., 2017) was used to

276   construct our model. Parameters of the semantic layer of the model were calibrated to

277   achieve feature extraction and classification of stream images. The image size was first

278   rescaled from 2560×1440 to 227×227 to facilitate the migration of trained AlexNet. A

279   227×227×3 (length×width×color) matrix was retrieved from each image as the model

280   input. There were five built-in convolutional layers, using a 3×3 convolution kernel and

281   a 3×3 pooled kernel. We replaced the last three layers of AlexNet with a full-connection

282   layer, a softmax layer, and a classification layer, leaving all other layers intact. The

283   parameters of the full-connection layer were set according to the number of selected

284   discharge values. The ReLU function was used as the convolutional layer activation

285   function to extract and pass on the water coverage features. The SoftMax function was

286   the activation function of the output layer, and the extracted feature vectors were

287   compressed under each discharge label. The probability that a stream image falls into a

288   discharge label was calculated as

$$P(y|x) = \frac{e^{h(x,y_i)}}{\sum_{i=1}^{n} e^{h(x,y_i)}} \qquad (6)$$

290   where x is the feature vector extracted by CNN, y is the discharge label, n is the number

291   of labels, $h(x, y_i)$ is the linear connectivity function. The training method for CNN

292   was stochastic gradient descent with momentum, with 15 samples in small batches, a

293   maximum number of rounds of 10, a validation frequency of 3 epochs, and an initial

294   learning rate of 0.00005. The samples were shuffled in every epoch. The loss function

295   for discharge classification was Cross-Entropy Loss, as

$$L = -\frac{1}{N} \sum_{i=1}^{N} \sum_{c=1}^{C} y_{i,c} \log(p_{i,c}) \qquad (7)$$

297   where L is the value of loss, N is the number of samples, C is the number of discharge

298   classes, $y_{i,c}$ represents the value of the true label for the ith sample in the cth class using

299   one-hot encoding, and $p_{i,c}$ represents the probability of ith sample belonging to c^{th}

300   class calculated by CNN.

301

302   **2.5.2 Convolutional Neural Network coupled with Support Vector Machine**

303   **(CNN+SVM)**

304   SVM is a machine learning method based on structural risk minimization and Vapnik–

305   Chervonenkis (VC) dimension theory (Cortes and Vapnik, 1995). It has been widely

306   used in image processing, pattern recognition, fault diagnosis, prediction and

307 classification (Burges, 1998), which can help to capture key samples and eliminate

308 redundant samples by finding the optimal hyperplane. Compared with neural networks,

309 which rely on large training samples and tend to fall into local optima, SVM can achieve

310 global optima with a simpler model structure (Hanczar et al., 2010; Matykiewicz and

311 Pestian, 2012). However, the SVM-based classifier requires manual input of image

312 features. Therefore, we coupled CNN and SVM to achieve automatic discharge

313 classification. Image features extracted by CNN (i.e., the output of the 5th CNN pooling

314 layer) were fed into SVM classifiers to calculate discharge. The extracted image

315 features were coded with "one-vs-all" scheme, and the linear kernel function was

316 selected for SVM classifier with hinge loss.

317

318 **2.4.3 Convolutional Neural Network coupled with Random Forest (CNN+RF)**

319 RF (Tin Kam, 1995) is a flexible machine-learning algorithm that combines the output

320 of multiple decision trees to reach a single result. Each decision tree depends on the

321 values of a random vector sampled independently and with the same distribution for all

322 trees in the forest (Breiman, 2001; Panda et al., 2009). It is an integrated algorithm of

323 the Bagging type (Aslam et al., 2007) that combines multiple weaker classifiers, and

324 the final result is obtained by voting or averaging to improve accuracy and

325 generalization performance. We here used an RF with 350 decision trees and five

326 decision leaves. The coupling method of CNN+RF is similar to CNN+SVM, using the

327 same pooling outputs of CNN as the inputs of RF discharge classifiers.

328

2.6 Model evaluation metrics

330 The performance of discharge classification models was measured by four widely used

331 metrics, including classification accuracy, F1 score, coefficient of determination (R^2),

332 and root mean square error (RMSE).

333 (1) Accuracy:

334
$$Accuracy = \frac{\sum_{i=1}^{k} TP_i}{N} \tag{8}$$

335 where TP_i is the number of correctly classified samples in the ith discharge class; N is

336 the total number of samples; k is the number of discharge classes.

337 (2) F1 score:

338
$$F1 = \frac{2 \times Precision \times Recall}{Precision + Recall} \tag{9}$$

339 where $Precision$ is the ratio of true positive classification (TP_i) to the sum of TP_i and

340 the number of misclassified samples with the ith discharge simulated by a model (FP_i);

341 $Recall$ is the ratio of TP_i to the sum of TP_i and the number of misclassified samples

342 with the observed i^{th} discharge (FN_i), calculated as

343
$$Precision = \sum_{i=1}^{k} \frac{n_i}{N} \times \frac{TP_i}{TP_i + FP_i} \tag{10}$$

344
$$Recall = \sum_{i=1}^{k} \frac{n_i}{N} \times \frac{TP_i}{TP_i + FN_i} \tag{11}$$

345 where n_i is the number of samples that fall in the ith class.

346 (3) R²

347
$$R^2 = 1 - \frac{\sum_{j=1}^{N} (y_j - \hat{y}_j)^2}{\sum_{j=1}^{N} (y_j - Y)^2} \tag{12}$$

348 where y_j and $\hat{y}_j$ are the observed and simulated discharge, respectively; Y is the mean

349   discharge.

350   (4) RMSE

351
$$RMSE = \sqrt{\frac{1}{N}\sum_{j=1}^{N}(y_j - \hat{y}_j)^2} \quad (13)$$

352   3 Results

353   3.1 Correlation analysis

354   Traversing the common algebraic combinations of the three colors, we found that

355    $-\bar{R} + 7.5\bar{G} - 6.5\bar{B}$ ($\bar{R}$, $\bar{G}$, $\bar{B}$ are the mean values of red, green and blue channels of

356   an image, respectively) had a spearman correlation coefficient of 0.67 with discharge

357   (p-value < 0.01), indicating that the discharge is significantly correlated with the color

358   combination value at the 99% confidence level (**Fig. 5**). Such result suggests that

359   discharge conditions are embedded in RGB information of mountain streams to some

360   extent, which could be further retrieved and refined by CNN models.
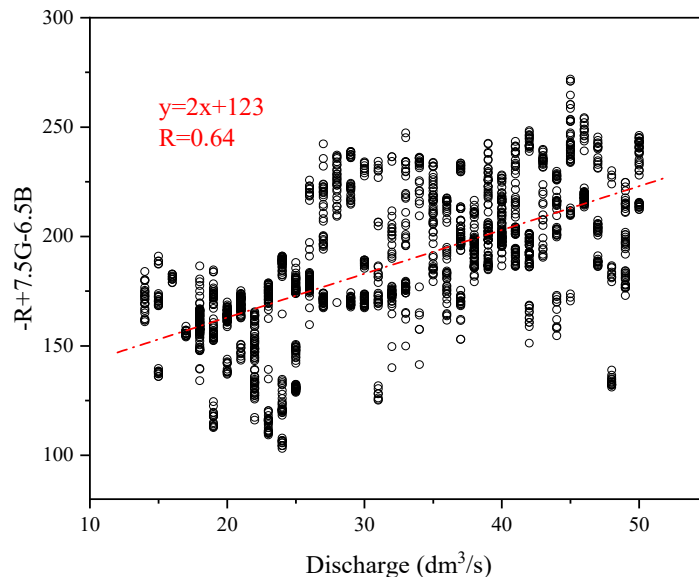
361

362   **Figure 5.** Correlation between RGB color values and corresponding discharges.

363

3.2 Effectiveness of automated image categorization

Most of the previous image-based studies only selected unblemished images for discharge or velocity monitoring, which resulted in poor model performance under environmental disturbances (Leduc et al., 2018; Chapman et al., 2020; Herzog et al., 2022). In this study, we also included samples under the influence of vegetation shadows and water reflection for model training. We selected approximately 100 stream images corresponding to each discharge volume (at the interval of 0.001 m³/s) from the pre-processed samples (3168 images in total). The databases of "Good quality", "Middle shadow", "Below shadow", and "Water reflection" were approximately sampled in the ratio of 7:0.6:1.4:1 (2146:244:437:341 images) to ensure the representation of different environmental conditions. The samples were distributed evenly in each discharge interval to avoid bias towards particular discharge conditions and enhance model performance on high and low flows (Wang et al., 2023).

Fig. 6 demonstrates the difference in accuracy of monitoring discharge by the defective images, using two sets of models trained with only "Good quality" images and samples filtered by automated image categorization, respectively. Results derived from the three discharge classification models and three color-enhancing methods consistently suggest that the procedure of automated image categorization can significantly improve model performance in apprehending defective images. Classification accuracy of the models trained with only "Good quality" samples staggered between 11.8%-18.7%, while the accuracy of the models trained after

385 automated image categorization was higher than 79.0% (79.0%-97.4%) regardless of

386 the choices of color processing method and deep learning model. The average

387 difference in accuracy between the two sets of training samples reached 73.9%. The

388 proportionate inclusion of defective images with vegetation shadow and water surface

389 reflection enhances the anti-interference ability of the models in complex environments.

390
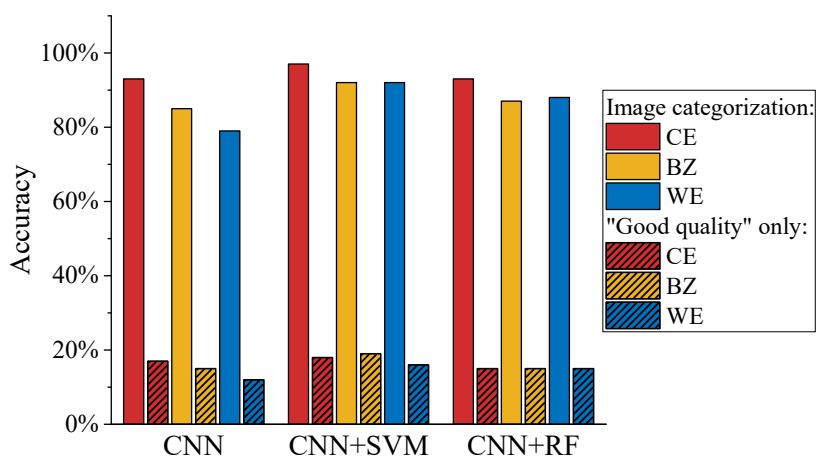
391

392 **Figure 6.** Accuracy of discharge classification of images under environmental

393 disturbances. Bars with and without patterns show the results using the models trained

394 with only "Good quality" samples and samples after automated image categorization,

395 respectively. Color enhancement methods include Color Enhanced (CE), Binarization

396 (BZ), and Water-color Enhanced (WE).

397

398 3.3 Model training and validation

399 After the treatments of color-enhancing, image denoising, and automated image

400 categorization, the images were randomly divided into training and validation sets by

401 the ratio of 7:3, and then used for model training and validation, respectively.

402

3.3.1 Loss changes

The changes in training and validation loss of the CNN models driven by three types of color-enhanced images are demonstrated in **Fig. 7**. In the initial twenty epochs, the training loss values decreased rapidly from 7.70 to 3.73 (Color Enhanced), from 5.91 to 3.73 (Binarization), and from 5.41 to 3.80 (Water-color Enhanced), respectively. Subsequently, the decreasing rates slowed during the following 1000 epochs, averaging around -0.0027 to -0.0030 per epoch. The loss value usually stabilizes after 1000 epochs in CNN training (Keskar et al., 2016). In our case, the loss value began to flatten after the 1300th epoch, signifying convergence towards a consistent loss value below 1.00 across all three color-enhancing methods. Therefore, we set the maximum training epochs to 1470 to ensure model performance while avoiding overfitting.

The proximity between the training and validation loss changes at the final few epochs is an important indicator that the model is not suffering from overfitting. A commonly acknowledged benchmark of such proximity is approximately 0.1 to 0.2 (Heaton, 2018). In our CNN models, the validation loss values at the final epoch were 0.60, 0.78, and 0.63, respectively, which were 0.19, 0.08, and 0.07 lower than the corresponding training loss. Such results suggest that the models did not suffer from overfitting or underfitting.

421
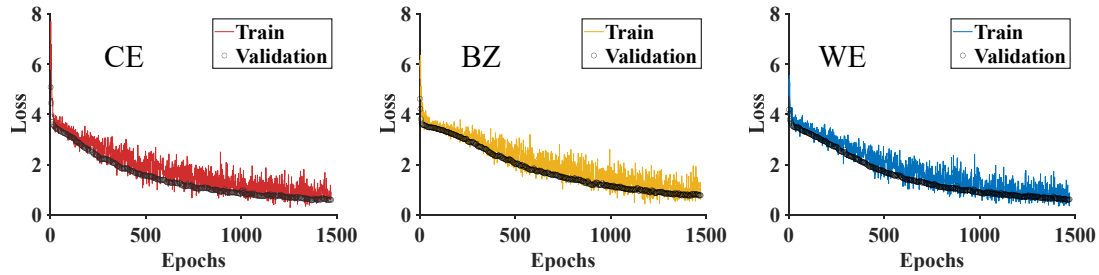
Figure 7. Changes in training and validation loss of the models driven by three types of color-enhanced images. Color enhancement methods include Color Enhanced (CE), Binarization (BZ), and Water-color Enhanced (WE).

3.3.2 Comparison of discharge models

The heap map (**Fig. 8**) visualizes the performance of different models in classifying the validation image set with three tested color-enhancing methods under different environmental conditions. Results show that all three models (i.e., CNN, CNN+SVM, CNN+RF) can achieve satisfactory performance on discharge classification. The R^2 under all environmental conditions was greater than 0.97, suggesting that the simulated discharge were significantly correlated to the flowmeters' measurement. The comparison of model performance generally shows consistency under different environmental conditions. Among the three models, CNN is more likely to over- or under-estimate discharge than both CNN+SVM and CNN+RF, with accuracy and F1 score 8.6~13.4% and 0.084~0.115 lower than CNN+SVM and CNN+RF, respectively. CNN+RF achieved the best fit with the lowest RMSE. With all environmental conditions taken into account, CNN+SVM shows the best overall performance with the highest accuracy of 88.6%, the highest F1 score of 0.878, and the lowest RMSE of 1.08

441   dm^3/s. Such results could be related to the size of our samples and the characteristics of

442   the features extracted by deep layers of CNN. The features extracted from stream

443   images under one specific flow discharge show similarities, which highlights the

444   SVM's capability in classifying the embeddings from small samples with linear features.

445

446   **3.3.3 Comparison of color-enhancing methods**

447   Among the three tested color-enhancing methods, the Color Enhanced approach

448   generally shows the best performance in discharge classification. Models driven by

449   Color Enhanced images achieved higher accuracy (+2.3%~+7.4%), higher F1 score

450   (+0.033~+0.067), and lower RMSE (–0.068 ~ –0.415 dm^3/s) than those driven by

451   images processed with Binarization and Water-color Enhanced. This is partly due to the

452   different treatments in the edges of the water body. Binarization and Water-color

453   Enhanced relatively cause larger deviation from the real edges, while Color Enhanced

454   retains the image information to the maximum extent. Binarization reduces the cost of

455   computation and data storage by transforming raw stream images into binary images,

456   and thus facilitates real-time monitoring by embedded end-to-end devices (e.g., mobile

457   phones) with insufficient computing power (Shi et al., 2019). Considering that the color

458   and texture of the water surface vary significantly with discharge volumes while the

459   background is relatively stable, we proposed the Water-color Enhanced approach that

460   only processes color information within the water body. In our experiment, it took only

461   0.0154s to recognize flow discharge from one Binarization image with an Intel (R) Core

462   (TM) i7-10750H CPU, which was 36% and 22% faster than that of Color Enhanced

463   and Water-color Enhanced images, respectively. Such results suggest that it is

464   beneficial to retain the background information to the maximum extent and include the

465   non-water parts of mountain streams in image processing. However, future applications

466   of image-based discharge monitoring need to strike a balance between accuracy and

467   speed when choosing color processing methods.

468

469

470
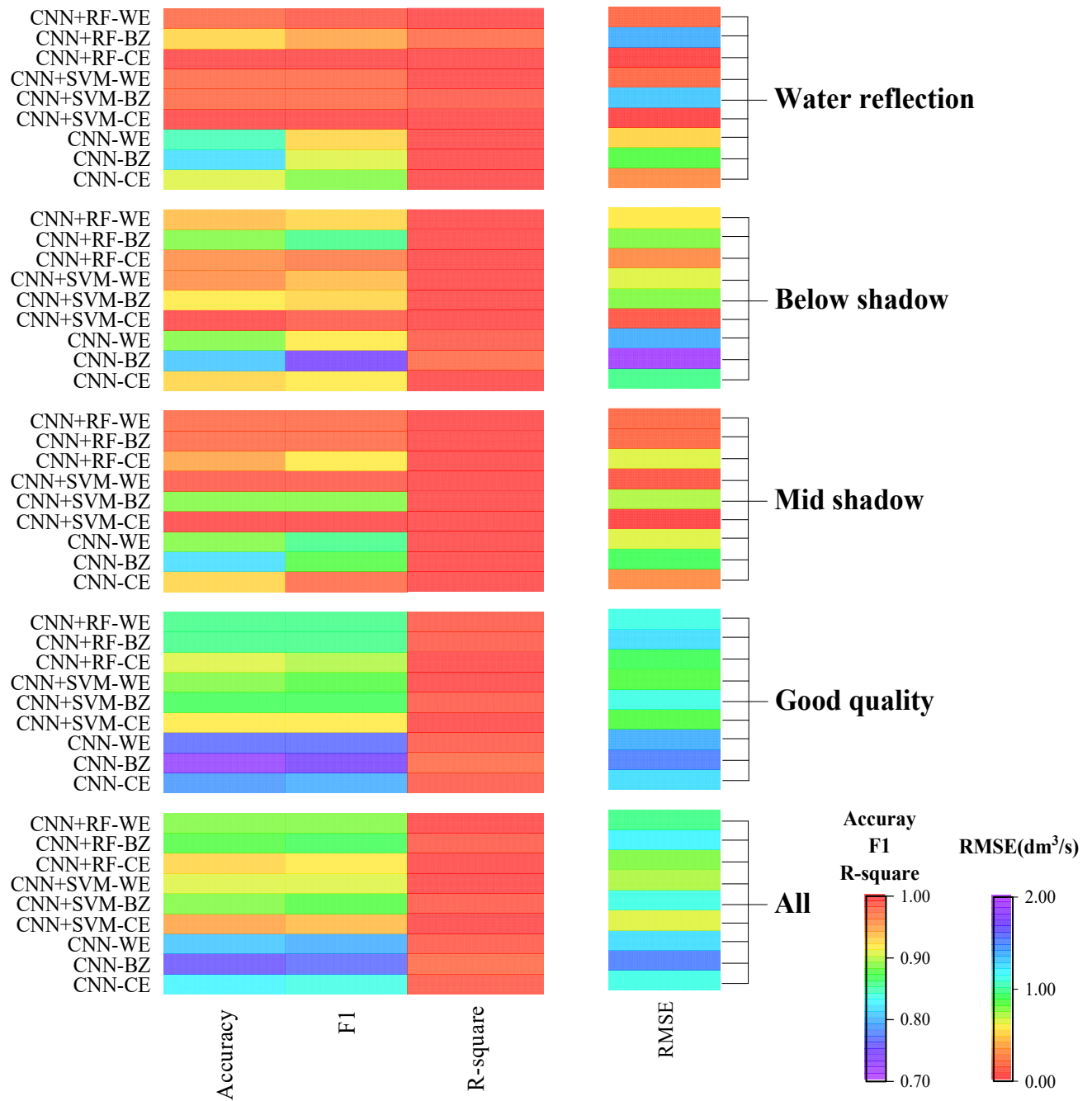
471

472

473 **Figure 8.** Performance of discharge classification models under different

474 environmental conditions. Color enhancement methods include Color Enhanced (CE),

475   Binarization (BZ), and Water-color Enhanced (WE).

476

4 Discussion

478   The existing image-based methods usually rely on either the estimations of flow

479   velocity and cross-section area or assumptions on stage-discharge correlation (Tauro et

480   al., 2017; Leduc et al., 2018; Davids et al., 2019; Li et al., 2019). The first type of

481   method uses image-derived surface velocity to estimate sub-sectional mean streamflow

482   velocity and spatial integration of discharge (Le Coz et al., 2012). The difficulties in

483   capturing cross-sectional characteristics and the relationship between flow velocity and

484   water depth limit their application in small mountain streams. The second type of

485   method retrieves river geometry directly through remote sensing, yet the accuracy is

486   primarily determined by the empirical assumptions on the relationships among water

487   depth, velocity, and discharge (Gleason and Smith, 2014; Young et al., 2015). In this

488   study, we proposed a new camera-based method to directly establish the relationship

489   between the RGB matrixes of stream images and the classification probabilities of

490   discharge. The unique merit of the CNN-based model is its capability in automatically

491   extracting and refining discharge-related features from image samples, which improves

492   the accuracy and applicability of the model. Previous attempts suggest that the selection

493   of image features can significantly affect the performance on classification of stream

494   images (Tauro et al., 2014). For example, Chapman et al. (2020) manually extracted

495   features from pre- and post-weir images and used them as the inputs of machine

496 learning models. However, the dominant image features relating to stream discharge

497 could vary across different environments (e.g., topography, vegetation on river banks,

498 water quality), limiting the transferability of such manually identified features.

499 Weather conditions (e.g., sun position, fog, rain) are the most common difficulties

500 that reduce picture quality (Leduc et al., 2018). Therefore, we designed an automated

501 procedure for categorizing samples by their brightness and saturation: (a) select four

502 areas in the image as detection areas, (b) eliminate images with insufficient light or

503 raindrops on the lens, (c) identify thresholds and classify the remaining images into four

504 categories for further model training, including the images under the influence of

505 vegetation shadow and overexposure caused by water reflection in certain angles. Such

506 inclusion and categorization of defective samples have significantly enhanced the anti-

507 interference ability of the model, facilitating uninterrupted discharge monitoring

508 through the daytime. These factors and the thresholds of brightness and saturation are

509 site-specific and require manual trials to identify them. However, after adequate initial

510 calibration, an established model can be used for the same site for extended periods and

511 repeated installations of camera systems.

512 The training and validation of deep learning models require a large number of

513 representative samples (He et al., 2016). We collected a total of 7757 image samples

514 from July 20th to September 27th, 2022, and 3168 images were used for model training

515 and validation after image screening and categorization. Although we executed an

516 effective automatic categorization procedure on the acquired image samples, it is

undeniable that the training and validation sets didn't cover all environmental

disturbances. For example, the time of sunrise and sunset, the appearance of water

surface reflections, and the coverage of vegetation shadows are affected by the angles

of sunlight and vary with seasons. With sufficient artificial lighting or installation of a

night-vision infrared camera (Royem et al., 2012), the images during nighttime can also

be used for discharge monitoring after training. More image samples are needed to

enrich the representativeness of the model in further studies. Another limitation is that

we have focused on low and average flow conditions in the model training due to the

lack of high-quality flood samples. In tropical and subtropical mountain streams of

southern China, floods usually occur during rainstorms and only last for a short time.

Heavy rainfalls constantly block the camera lens with raindrops, and the rapid

streamflow movement during heavy rainfall tends to cause blurred images, which can

only be partly improved by increasing the shutter speed and adjusting the camera

position.

5 Conclusions

The results demonstrate the effectiveness of a novel method for discharge monitoring

of mountain streams using deep learning and a low-cost solar-powered commercial

camera (approximately \$200). The discharge-relevant stream features embedded in a

large number of RGB images can be implicitly recognized and retrieved by CNN to

achieve continuous discharge monitoring. Coupling CNN and traditional machine

538   learning methods can potentially improve model performance in discharge

539   classification to various extents. In this case, the accuracy of CNN+SVM and CNN+RF

540   were 9.1%~14.4% higher, while the F1 score were 0.084~0.115 higher compared to

541   CNN. Proper image pre-processing and categorization can largely enhance the

542   applicability of image-based discharge monitoring. In an environment under complex

543   disturbances such as mountain streams, image quality is constantly interfered with by

544   shadows of vegetation on the river banks. The automated image categorization

545   procedure can effectively recognize discharge from defective images by filtering

546   samples under different conditions and improve model robustness. The comparison of

547   the three color-enhancing approaches also confirms the importance of including the

548   non-water parts (e.g., large rocks) and retaining the background information to the

549   maximum extent in the image analysis.

550   The proposed method provides an inexpensive and flexible alternative apparatus for

551   continuous discharge monitoring at rocky upstream mountain streams, where it is

552   challenging to identify the cross-section shape or establish a stable stage-discharge

553   relationship. Site-specific field data is needed to identify the criteria for image

554   categorization and model validation. However, it circumvents the potential errors in

555   assuming cross-section characteristics, such as the relationship between water depth

556   and flow velocity, and represents a new direction for applying deep learning techniques

557   in acquiring high-frequency discharge data through image analysis.

558

Code/Data availability

The code and data are available upon request from the corresponding author.

Author contribution

KD and CF conceptualized the experiments. GY, ZZ, and QZ curated the data. All authors participated in the investigation. CF, GY, ZZ, and QZ wrote the original draft and visualized the data. KD reviewed and edited the final version of the manuscript.

Competing interests

The authors declare no competing interests.

Acknowledgments

This work was supported by the National Key Research and Development Program of China (2021YFC3001000; 2021YFC3200205), the National Natural Science Foundation of China (52379032; 51909285), the Guangdong Basic and Applied Basic Research Foundation (2023A1515012241), and the Guangdong Provincial Department of Science and Technology (2019ZT08G090).

References

Abdullah-Al-Wadud, M., Kabir, M. H., Dewan, M. A. A., and Chae, O.: A Dynamic Histogram Equalization for Image Contrast Enhancement, IEEE Transactions on Consumer Electronics, 53, 593-600, 10.1109/TCE.2007.381734, 2007.

Aslam, J. A., Popa, R. A., and Rivest, R. L.: On estimating the size and confidence of a

579 statistical audit, Proceedings of the USENIX Workshop on Accurate Electronic

580   Voting Technology, Boston, MA, 10.5555/1323111.1323119, 2007.

581 Breiman, L.: Random Forests, Machine Learning, 45, 5-32, 10.1023/A:1010933404324,

582   2001.

583 Burges, C. J. C.: A Tutorial on Support Vector Machines for Pattern Recognition, Data

584   Mining and Knowledge Discovery, 2, 121-167, 10.1023/A:1009715923555, 1998.

585 Canziani, A., Paszke, A., and Culurciello, E.: An Analysis of Deep Neural Network

586   Models for Practical Applications, ArXiv, abs/1605.07678, 7-14,

587   10.48550/arXiv.1605.07678, 2016.

588 Carlisle, D., Grantham, T. E., Eng, K., and Wolock, D. M.: Biological relevance of

589   streamflow metrics: Regional and national perspectives, Freshwater Science, 36,

590   927-940, 10.1086/694913, 2017.

591 Chang, F., Hong, W., Zhang, T., Jing, J., and Liu, X.: Research on Wavelet Denoising

592   for Pulse Signal Based on Improved Wavelet Thresholding, 2010 First International

593   Conference on Pervasive Computing, Signal Processing and Applications, Harbin,

594   China, 17-19 Sept. 2010, 564-567, 10.1109/PCSPA.2010.142, 2010.

595 Chapman, K. W., Gilmore, T. E., Chapman, C. D., Mehrubeoglu, M., and Mittelstet, A.

596   R.: Camera-based Water Stage and Discharge Prediction with Machine Learning,

597   Hydrol. Earth Syst. Sci. Discuss., 2020, 1-28, 10.5194/hess-2020-575, 2020.

598 Cheng, H. D. and Shi, X. J.: A simple and effective histogram equalization approach to

599   image enhancement, Digital Signal Processing, 14, 158-170,

600   10.1016/j.dsp.2003.07.002, 2004.

601 Clarke, R. T.: Uncertainty in the estimation of mean annual flood due to rating-curve

602   indefinition, Journal of Hydrology, 222, 185-190, 10.1016/S0022-1694(99)00097-9,

603   1999.

604 Cortes, C. and Vapnik, V.: Support-vector networks, Machine Learning, 20, 273-297,

605   10.1007/bf00994018, 1995.

606 Council, N. R.: Assessing the national streamflow information program, National

607   Academies Press, 176 pp., 10.17226/10967, 2004.

608   Czuba, J. A., Foufoula-Georgiou, E., Gran, K. B., Belmont, P., and Wilcock, P. R.:

609   Interplay between spatially explicit sediment sourcing, hierarchical river-network

610   structure, and in-channel bed material sediment transport and storage dynamics,

611   Journal of Geophysical Research: Earth Surface, 122, 1090-1120,

612   10.1002/2016jf003965, 2017.

613   Davids, J. C., Rutten, M. M., Pandey, A., Devkota, N., van Oyen, W. D., Prajapati, R.,

614   and van de Giesen, N.: Citizen science flow – an assessment of simple streamflow

615   measurement methods, Hydrology and Earth System Sciences, 23, 1045-1065,

616   10.5194/hess-23-1045-2019, 2019.

617   Deweber, J. T., Tsang, Y. P., Krueger, D. M., Whittier, J. B., Wagner, T., Infante, D. M.,

618   and Whelan, G.: Importance of Understanding Landscape Biases in USGS Gage

619   Locations: Implications and Solutions for Managers, Fisheries, 39, 155-163,

620   10.1080/03632415.2014.891503, 2014.

621   Finlayson, G. D., Hordley, S. D., and Drew, M. S.: Removing Shadows from Images,

622   Computer Vision — ECCV 2002, Berlin, Heidelberg, 2002, 823-836, 10.1007/3-

623   540-47979-1_55, 2002.

624   Fujita, I., Muste, M., and Kruger, A.: Large-scale particle image velocimetry for flow

625   analysis in hydraulic engineering applications, Journal of Hydraulic Research, 36,

626   397-414, 10.1080/00221689809498626, 2010.

627   Fujita, I., Watanabe, H., and Tsubaki, R.: Development of a non-intrusive and efficient

628   flow monitoring technique: The space-time image velocimetry (STIV), International

629   Journal of River Basin Management, 5, 105-114, 10.1080/15715124.2007.9635310,

630   2007.

631   Gershon, R., Jepson, A. D., and Tsotsos, J. K.: Ambient illumination and the

632   determination of material changes, J Opt Soc Am A, 3, 1700-1707,

633   10.1364/josaa.3.001700, 1986.

634   Gleason, C. J. and Smith, L. C.: Toward global mapping of river discharge using

635   satellite images and at-many-stations hydraulic geometry, Proceedings of the

636   National Academy of Sciences, 111, 4788-4791, 10.1073/pnas.1317606111, 2014.

637   Hanczar, B., Hua, J., Sima, C., Weinstein, J., Bittner, M., and Dougherty, E. R.: Small-

638   sample precision of ROC-related estimates, Bioinformatics, 26, 822-830,

639   10.1093/bioinformatics/btq037, 2010.

640   Hannah, D. M., Demuth, S., van Lanen, H. A. J., Looser, U., Prudhomme, C., Rees, G.,

641   Stahl, K., and Tallaksen, L. M.: Large-scale river flow archives: importance, current

642   status and future needs, Hydrological Processes, 25, 1191-1200, 10.1002/hyp.7794,

643   2011.

644   He, K., Zhang, X., Ren, S., and Sun, J.: Deep residual learning for image recognition,

645   Proceedings of the IEEE conference on computer vision and pattern recognition, Las

646   Vegas, NV, USA, 770-778, 10.1109/cvpr.2016.90, 2016.

647   Heaton, J.: Ian Goodfellow, Yoshua Bengio, and Aaron Courville: Deep learning: The

648   MIT Press, Genetic programming and evolvable machines, 19, 305-307,

649   10.1007/s10710-017-9314-z, 2018.

650   Herzog, A., Stahl, K., Blauhut, V., and Weiler, M.: Measuring zero water level in stream

651   reaches: A comparison of an image-based versus a conventional method,

652   Hydrological Processes, 36, e14234, 10.1002/hyp.14658, 2022.

653   Jiang, P. T., Zhang, C. B., Hou, Q., Cheng, M. M., and Wei, Y.: LayerCAM: Exploring

654   Hierarchical Class Activation Maps for Localization, IEEE Transactions on Image

655   Processing, 30, 5875-5888, 10.1109/TIP.2021.3089943, 2021.

656   Karvonen, J.: Virtual radar ice buoys – a method for measuring fine-scale sea ice drift,

657   The Cryosphere, 10, 29-42, 10.5194/tc-10-29-2016, 2016.

658   Kasuga, K., Hachiya, H., and Kinosita, T.: Quantitative Estimation of the Ultrasound

659   Transmission Characteristics for River Flow Measurement during a Flood, Japanese

660   Journal of Applied Physics, 42, 3212-3215, 10.1143/jjap.42.3212, 2003.

661   Keskar, N., Mudigere, D., Nocedal, J., Smelyanskiy, M., and Tang, P.: On Large-Batch

662   Training for Deep Learning: Generalization Gap and Sharp Minima, arXiv preprint

arXiv:1609.04836, 10.48550/arXiv.1609.04836, 2016.

Kim, W., Roh, S.-H., Moon, Y., and Jung, S.: Evaluation of Rededge-M Camera for Water Color Observation after Image Preprocessing, Journal of the Korean Society of Surveying Geodesy Photogrammetry and Cartography, 37, 167-175, 10.7848/ksgpc.2019.37.3.167, 2019.

Krizhevsky, A., Sutskever, I., and Hinton, G. E.: ImageNet classification with deep convolutional neural networks, Communications of the ACM, 60, 84-90, 10.1145/3065386, 2017.

Le Coz, J., Camenen, B., Peyrard, X., and Dramais, G.: Uncertainty in open-channel discharges measured with the velocity–area method, Flow Measurement and Instrumentation, 26, 18-29, 10.1016/j.flowmeasinst.2012.05.001, 2012.

LeCun, Y., Bengio, Y., and Hinton, G.: Deep learning, Nature, 521, 436-444, 10.1038/nature14539, 2015.

Leduc, P., Ashmore, P., and Sjogren, D.: Technical note: Stage and water width measurement of a mountain stream using a simple time-lapse camera, Hydrology and Earth System Sciences, 22, 1-11, 10.5194/hess-22-1-2018, 2018.

Li, W., Liao, Q., and Ran, Q.: Stereo-imaging LSPIV (SI-LSPIV) for 3D water surface reconstruction and discharge measurement in mountain river flows, Journal of Hydrology, 578, 124099, 10.1016/j.jhydrol.2019.124099, 2019.

Matykiewicz, P. and Pestian, J.: Effect of small sample size on text categorization with support vector machines, Publication History, 193-201 pp., 10.5555/2391123.2391149, 2012.

McMillan, H., Freer, J., Pappenberger, F., Krueger, T., and Clark, M.: Impacts of uncertain river flow data on rainfall-runoff model calibration and discharge predictions, Hydrological Processes: An International Journal, 24, 1270-1284, 10.1002/hyp.7587, 2010.

Noto, S., Tauro, F., Petroselli, A., Apollonio, C., Botter, G., and Grimaldi, S.: Low-cost stage-camera system for continuous water-level monitoring in ephemeral streams,

Hydrological Sciences Journal, 67, 1439-1448, 10.1080/02626667.2022.2079415, 2022.

Panda, B., Herbach, J., Basu, S., and Bayardo, R.: PLANET: Massively parallel learning of tree ensembles with MapReduce, PVLDB, 2, 1426-1437, 10.14778/1687553.1687569, 2009.

Royem, A. A., Mui, C. K., Fuka, D. R., and Walter, M. T.: Technical Note: Proposing a Low-Tech, Affordable, Accurate Stream Stage Monitoring System, Transactions of the ASABE, 55, 2237-2242, 10.13031/2013.42512, 2012.

Sauvola, J. and Pietikäinen, M.: Adaptive document image binarization, Pattern Recognition, 33, 225-236, 10.1016/s0031-3203(99)00055-2, 2000.

Shi, W., Jiang, F., Liu, S., and Zhao, D.: Image Compressed Sensing using Convolutional Neural Network, IEEE Trans Image Process, 29, 375-388, 10.1109/TIP.2019.2928136, 2019.

Tauro, F., Grimaldi, S., and Porfiri, M.: Unraveling flow patterns through nonlinear manifold learning, PLoS One, 9, e91131, 10.1371/journal.pone.0091131, 2014.

Tauro, F., Piscopia, R., and Grimaldi, S.: Streamflow Observations From Cameras: Large-Scale Particle Image Velocimetry or Particle Tracking Velocimetry?, Water Resources Research, 53, 10374-10394, 10.1002/2017wr020848, 2017.

Tauro, F., Tosi, F., Mattoccia, S., Toth, E., Piscopia, R., and Grimaldi, S.: Optical Tracking Velocimetry (OTV): Leveraging Optical Flow and Trajectory-Based Filtering for Surface Streamflow Observations, Remote Sensing, 10, 2010, 10.3390/rs10122010, 2018.

Tin Kam, H.: Random decision forests, Proceedings of 3rd International Conference on Document Analysis and Recognition, Montreal, QC, Canada, 14-16 Aug. 1995, 278-282 vol.271, 10.1109/ICDAR.1995.598994, 1995.

Tsubaki, R.: On the Texture Angle Detection Used in Space-Time Image Velocimetry (STIV), Water Resources Research, 53, 10908-10914, 10.1002/2017wr021913, 2017.

Wang, R., Chaudhari, P., and Davatzikos, C.: Bias in machine learning models can be

719   significantly mitigated by careful training: Evidence from neuroimaging studies,

720   Proceedings of the National Academy of Sciences, 120, e2211613120,

721   10.1073/pnas.2211613120, 2023.

722   Yorke, T. H. and Oberg, K. A.: Measuring river velocity and discharge with acoustic

723   Doppler profilers, Flow Measurement and Instrumentation, 13, 191-195,

724   10.1016/s0955-5986(02)00051-1, 2002.

725   Young, D. S., Hart, J. K., and Martinez, K.: Image analysis techniques to estimate river

726   discharge using time-lapse cameras in remote locations, Computers & Geosciences,

727   76, 1-10, 10.1016/j.cageo.2014.11.008, 2015.

728   Zhang, D.: Fundamentals of Image Data Mining, Analysis, Features, Classification and

729   Retrieval, Springer, 7, 35-44, 10.1007/978-3-030-17989-2, 2019.

730